2018 Annual American Control Conference (ACC)
June 27–29, 2018. Wisconsin Center, Milwaukee, USA

Passivity-based Iterative Learning Control Design for Selective Laser Melting

Michael J.B. Spector[1], Yijie Guo[1], Souvik Roy[1], Max O. Bloomfield[2], Antoinette Maniatty[1] and Sandipan Mishra[1]

Abstract— **Selective laser melting (SLM) is an additive manufacturing process that creates 3D parts through layer by layer melting and fusion of a metal powder bed. Although a number of finite element models (FEM) have been developed that describe the coupled and complex physics associated with this process, they are typically not suitable for control algorithm design. In this manuscript, a control oriented reduced order model (ROM) to adequately capture these temperature dynamics is proposed and validated against high fidelity FEM simulations. Further, since the laser paths are often repetitive (or consist of repeating sub-trajectories), iterative learning control (ILC) algorithms can be used to obtain suitable laser power profiles to deliver desired temperature field profiles. However, the process is inherently multiple input single output (MISO), therefore, a suitable output is constructed in such a way so as to the make the system passive. A passivity-based ILC law is then designed to drive this synthesized output to a desired profile and a convergence criterion for this law derived. The proposed ILC update law is implemented on both models and the results are compared for a set of candidate laser paths. Finally, the ILC update law is implemented on the high-fidelity FEM to melt a ring geometry to demonstrate the capability of the ILC algorithm to generate optimal laser power profiles for creating complicated geometries on large powder beds.**

I. INTRODUCTION

There are tremendous opportunities for metal selective laser melting (SLM) in a variety of industries, including aerospace, tool manufacturing, and medicine [1]. However, making reliable, high quality parts has proven to be challenging. Generating suitable temperature profiles is one of the critical factors for creating consistent parts with low residual stresses and small feature sizes. Residual stress originates from a local phenomenon that affects the part as a whole. During the processing of an individual layer, a large thermal gradient is created when the powder bed locally melts and subsequently consolidates. This gradient causes both local, thermally-induced residual stress as well as a more global stress stemming from nonuniform, thermal expansion within the previously formed layers and substrate [2]. Similarly, controlling the melt pool shape directly affects the feature size of parts and the geometric tolerance. Therefore, optimizing (time-varying) parameters like the laser velocity and power can improve the performance of the process, from a geometric tolerance as well as residual stress standpoint.

The ability to optimize laser power and scan paths demands a grounded understanding of the evolution of temperature dynamics, as well as the manipulation of these temperature dynamics through the controllable inputs. During the in-layer SLM processing various radiative, convective, and conductive heat transfer mechanisms occur and are coupled with the metal melting, evaporating, ionizing, and solidifying [3], [4], [5]. Finite element models (FEM) have been developed to describe many of the dynamics associated with SLM [6], [7], [8] and have had significant success in replicating the laser melt pool dimensions and temperature fields seen in experiment by modeling the laser absorption, heat conduction, and solid/liquid phase transitions in the powder and substrate while ignoring other complex dynamics mentioned above. However, these complex, coupled partial differential equation are computationally intensive to solve, which limits the use of any control scheme for manufacturing applications. In addition, establishing the performance of these (closed loop) systems is notoriously challenging when a control scheme is introduced.

Several attempts have been made to demonstrate a variety of control schemes in experimental or simulated implementations of SLM. [9] provides a review of some of these publications. One of the seminal works in this area was done in [10], where a closed-loop PID control was used with either a pyrometer or a CMOS sensor for feedback measurement to maintain the geometry of the melt pool, which improved the dimensional accuracy of SLM built parts. More complex strategies that also employ melt pool geometry control have supported these findings [11]. All of these works were performed on experimental apparatus and do not provide provable stability or performance guarantees.

On the other hand, there has been some effort in Direct Energy Deposition (DED) manufacturing methods, which is a similar 3D printing method [12], towards development of lumped parameter models along with more advanced controls to improve part quality [13], [14], [15], [16]. By simplifying the coupled physics of DED, these models adequately capture the temperature and build height dynamics while minimizing computational complexity. Using these lumped parameter models as design tools, these approaches have successfully demonstrated control algorithms for tracking temperature dynamics, melt pool geometry, and layer height, among others. Of particular importance is the use of Iterative Learning Control (ILC) to adaptively control DED parame-

[1]Michael J.B. Spector, Yijie Guo, Souvik Roy, Antoinette Maniatty, and Sandipan Mishra are with the Mechanical, Aerospace, and Nuclear Engineering Department, Rensselaer Polytechnic Institute, Troy, NY 12180 USA {spectm2, guoy7, roys23, maniaa, mishrs2}@rpi.edu

[2]Max Bloomfield is with the Scientific Computation Research Center, Rensselaer Polytechnic Institute, Troy, NY 12180 USA bloom2@rpi.edu

ters. [14] used ILC to adjust DED parameters to guarantee consistent layer height.

ILC aims to improve tracking performance in repetitive processes by updating the feed forward control signal based on previous iterations' information. ILC algorithms can often achieve excellent tracking performance in spite of imperfect model knowledge and are well-suited to reject systematic repetitive disturbances [17]. Typically in SLM processing, most laser paths are repetitive or can be partitioned into several repeating segments. This repetition, in conjunction with the fact that SLM process models are difficult to determine, offers the opportunity to use ILC to learn from previous iterations in order to generate suitable laser power profiles for each path segment. These path segments will ultimately be stitched together. However, the scope of this paper is limited to determining the power profiles for individual segments. The stitching process has already been presented in other work [18].

In this work, an ILC algorithm is designed based on a proposed control-oriented model and validated through high fidelity FEM simulations. First, a control-oriented reduced order model (ROM) for the temperature dynamics of a single layer SLM process is proposed. Second, to leverage potential repetition during in-layer, layer-to-layer, and part-to-part SLM manufacturing, an ILC update law is designed to track a (weighted) averaged temperature field. Based on the strictly output-incremental passivity of the ROM, a sufficient convergence condition for the proposed ILC update law is proposed and proven. Finally, the ROM is validated against a high fidelity FEM developed by Roy et. al [6], and both models are used to demonstrate the performance of the aforementioned ILC update law for typical laser scan paths.

The paper is organized as follows: First the problem description is given in Sec.II. Second, the reduced order model of the SLM temperature dynamics is proposed in Sec. III, then the ILC update law is described in Sec. IV, the convergence criterion for the ILC update law and the corresponding proof are also presented in this section. Third, in V, the ROM is verified and validated with FEM simulation results and simulation results using the passivity-based ILC law are compared between the ROM and FEM. Finally, the ILC update law is shown to be capable of melting a more complex, 2D ring shape in the powder bed when using FEM simulations.

II. Problem Description

In SLM processing, the laser beam (with either fixed or varying power) moves along a predetermined path (ie. a square spiral path in Fig. 1) to melt the powder and substrate underneath into a dense monolithic layer. The surface is consequently covered with a new powder layer and the process is then repeated until the 3D part is created.

As mentioned in Sec. I, the scope of this paper is limited to a single repeating laser path segment with a prescribed velocity profile, and time duration of t_f. We assume that there is desired temperature field profile $T_d(t), \quad t \in [0, t_f]$, the controlled variable is the laser power $p(t), \quad t \in [0, t_f]$, and the measured temperature field is localized around the laser beam spot. The *feedforward control objective* is to design a learning law $p_{k+1}(t) = F(p_k(t), T_k(t), T_d(t))$ to achieve the tracking objective: $T_k(t) \to T_d(t)$ in some sense as $k \to \infty$, where k is the iteration number.

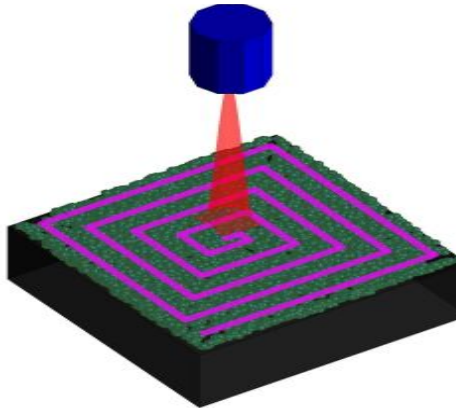

Fig. 1. Basic overview of the SLM process for one layer. The laser beam moves along a predetermined path (ie. a square spiral) to melt the powder bed into a dense, monolithic layer.

In order to design a feedforward learning control algorithm, we need a suitable model of the dynamics of SLM process. In the next section, an overview of some current modeling techniques are presented, the difficulty of using these techniques for control design are mentioned, and, subsequently, a control-oriented model is proposed.

III. Control-Oriented Modeling of SLM Temperature Dynamics

In this section, a brief introduction to SLM dynamics and existing high-fidelity FEM methods is provided. Using this as a foundation, a control-oriented model is proposed for control design.

A. High-Fidelity Modeling of SLM

There are many complex and coupled physical phenomena that occur during SLM processing of a single layer of powder that affect the temperature field, T. In spite of these complexities, many groups have had significant success reproducing powderbed temperature fields by neglecting the temperature dependencies of powder grains' optical properties, local powder grain kinetics and porosity, melt pool convection, possible atmospheric convection and plasma generation occurring near the powderbed surface, the increase in vapor pressure of the powder material before and after the powder reaches its evaporation temperature, as well as many other physical phenomena [7], [8], [19]. In addition, many of these models assume that the laser acts as a volumetric heat source that has been scattered and attenuated inside the powder layer. In these models, much of the powder bed temperature phenomena is thus captured by

$$\frac{\mathrm{d}H}{\mathrm{d}t} = \nabla(k\nabla T) + U, \tag{1}$$

where H represents the volumetric enthalpy of the powder layer and the platform beneath it; k represents the thermal conductivity of the powder, melt pool, the densified metal, and the substrate; and U is the volumetric heat source originating from the laser. H relates to T by

$$T = \begin{cases} \frac{H}{C_s}, & H \leq C_s T_m \\ T_m, & C_s T_m < H < C_s T_m + \mathscr{L} \\ T_m + \frac{(H - C_s T_m - \mathscr{L})}{C_l}, & H \geq C_s T_m + \mathscr{L} \end{cases}, \tag{2}$$

where C_s is the specific heat of the powder grains and platform; C_l is the specific heat of the materials in the liquid phase; T_m is the melting temperature of each material; and $\mathscr{L}$ is the latent heat of melting. The FEM used in the work, which is Roy et. al's FEM ([6]) without incorporating the melt consolidation of the powder layer, is also based on this set of equations.

However, the modeling of these SLM temperature dynamics is computationally intensive. This work shows that much of the temperature dynamics occurring below T_m can be captured with a simplified heat transfer equation applied onto a directed graph. The implementation of the simplified heat transfer equation using a directed graphs is presented next.

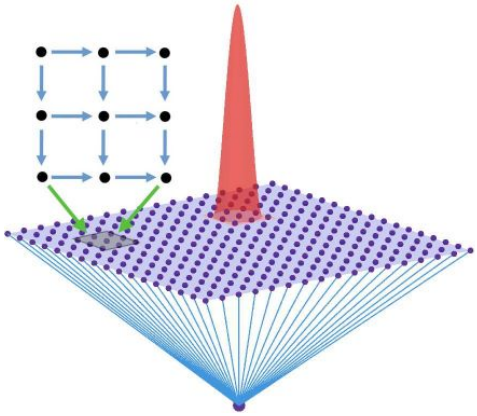

Fig. 2. Powderbed is discretized into $n_x \times n_y + 1$ nodes: $n \times m$ planar grid of powder nodes and a substrate node. Blue lines represent the thermal links between powder nodes and the substrate node. The inlay shows the local thermal links between a powder node and its nearest neighbor powder nodes. The red curve above the grid represents the distribution of absorbed laser power at time t.

B. Simplified Thermal Dynamics

The powder bed is first discretized into a grid of $N = n_x \times n_y$ grid of nodes where each node represents a volume of $\delta x \times \delta y \times \delta z$, as shown in Fig. 2. In this implementation of the ROM $n_x = n_y = n$ and $\delta x = \delta y$. The substrate is represented by a single node with its temperature being held at some T_{sub}. These nodes are connected together via links, which capture the heat transfer between nodes. Every powder node is directly linked to their nearest neighbors, which the inlay of Fig. 2 locally visualizes. In addition, each powder node is directly linked to the substrate node. Note that the direction of the links serves only as a sign convention in the incident matrix and does not indicate direction of heat transfer.

The simplified (discretized) heat transfer equation (without melting) for the i^{th} node can thus be written as

$$C_i \dot{T}_i(t) = \sum_{j \in N_i} k_{p,ij}\Big(T_j(t) - T_i(t)\Big) + k_{sub}\Big(T_{sub} - T_i\Big) + h_\infty\Big(T_\infty - T_i\Big) + b_i(t)p(t), \tag{3}$$

where $C_i\left[\frac{J}{K}\right]$ is the heat capacity of the i^{th} node, $T_i[K]$ is the temperature of the i^{th} node, N_i is the set of neighbors of the i^{th} node, $k_{p,ij}\left[\frac{W}{K}\right]$ is the conductivity between the i^{th} and j^{th} nodes, $k_{sub}\left[\frac{W}{K}\right]$ is the conductivity between nodes and the substrate node, T_{sub} is the temperature of the substrate which is held constant, $h_\infty\left[\frac{W}{K}\right]$ is the convection between nodes and ambient atmosphere, $T_\infty[K]$ is the temperature of the ambient atmosphere, b_i is the percentage of power absorbed at the i^{th} node from the laser power $p[W]$.

C. Control Oriented Reduced Order Model

Collecting (3) for each node, the dynamics of the temperature field can be written as:

$$C\dot{T}(t) = -DKD^T T(t) + K_{sub}(T_{sub} - T(t)) + H_\infty(T_\infty - T(t)) + B(t)p(t), \tag{4}$$

where $C \in \mathbb{R}^{N \times N}$ is a diagonal matrix with C_i being the i^{th} diagonal element, $T \in \mathbb{R}^N$ is the temperature field of the power bed, $D \in \mathbb{R}^{N \times q}$ is the directed incidence matrix where q is the number of links. $D(i,j)$ represents the relationship between node i and link j,

$$D(i,j) = \begin{cases} 1, & \text{node } i \text{ is the arrowhead of link } j \\ -1, & \text{node } i \text{ is the end of link } j \\ 0, & \text{link } j \text{ is not attached to node } i \end{cases}.$$

The diagonal matrix $K = k_p I^{m \times m}$ is a diagonal matrix where the i^{th} diagonal element describes the thermal conductivity of the i^{th} link, $K_{sub} = k_{sub} I^{N \times N}$ and $H_\infty = h_\infty I^{N \times N}$, which describe the thermal conductivity and convection to the substrate and ambient atmosphere, respectively.

The time-varying matrix $B(t) \in \mathbb{R}^{N \times 1}$ describes how much of the laser power, $p(t)$, at time t is absorbed by each element in the powder bed. As shown by the red curve overlaid on top of the powder layer in Fig. 2, the laser is incident on a local area of the powder surface. At time t, $B(t)p(t)$ inputs a fraction of $p(t)$ to nodes inside this area, while nodes outside of this area will absorb zero power. The overall laser transmission efficiency $\eta = \sum_i B_i(t)$, where $\eta \in [0,1]$ and i is the i^{th} element of $B(t)$. Without loss of generality, this is set to 1. Naturally, as the laser moves along the scan path, this distribution of where the laser heating is distributed changes. Hence, $B(t)$ is a time-varying vector directly related to the laser path and the laser power distribution.

The laser power distribution, Q, is formulated as a pseudo-Gaussian distribution. Q is centered at the laser center, and described below using r, as the local polar coordinate within the laser spot, and R, as the radius of the laser beam

$$Q = \frac{3}{\pi R^2}(1 - \frac{r^2}{R^2})^2. \tag{5}$$

IV. Iterative Learning Control Algorithm

In order to accurately track the desired temperature profile $T_d(t)$, we propose an ILC algorithm. ILC algorithms rely on tuning the current iteration control input based on previous iterations' input and the corresponding error information, as illustrated in Fig. 3.

As mentioned earlier, a single repeating laser path segment is repeated over $[0, t_f]$ and previous iterations' control input $p_{k-1}(t)$ and $e_{k-1}(t)$ are used to update the current iteration's control input p_k, where k is the iteration number, $e_k(t)$ is the tracking error in the kth iteration: $e_k(t) = y_k(t) - y_d(t)$. Ideally, we wish to drive the temperature field, $T(t) \in \mathbb{R}^N$, to $T_d(t) \in \mathbb{R}^N$. However, since we have only a single input, namely the laser power $p(t) \in \mathbb{R}$, we must design a single output $\tilde{y}(t) \in \mathbb{R}$ that can represent $T(t)$, y_d is the desired single output corresponding to $T_d(t)$. The *ILC control objective* is to design an ILC update law $p_k(t) = F(p_{k-1}(t), e_{k-1}(t)), t \in [0, t_f]$ to achieve the tracking objective $y_k(t) \to y_d(t)$ as $k \to \infty$.

In this section, a passivity based ILC update law is designed based on the control oriented ROM proposed in Section III.

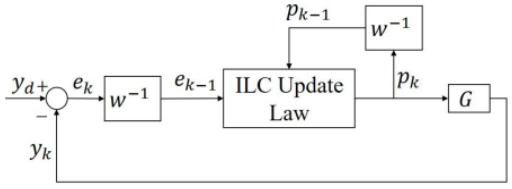

Fig. 3. Block Diagram of the ILC process, w^{-1} indicates one iteration delay, G is the plant of temperature dynamics.

A. Proportional ILC Update Law

In this work, a proportional ILC update law is used

$$p_{k+1}(t) = p_k(t) + Le_k(t) \tag{6a}$$
$$e_k(t) = y_d(t) - y_k(t), \tag{6b}$$

where $\tilde{y}(t) \in \mathbb{R}$ is the (synthesized) output, $L \in \mathbb{R}$ is the learning gain, $e_k(t) \in \mathbb{R}$ is the error, k is the iteration number, and $p_k(t) \in \mathbb{R}$ is the laser power.

As mentioned before, we must design a single output $\tilde{y}(t)$ that can represent $T(t)$. Further, choosing $\tilde{y}(t)$ as a passive output naturally endows robustness to any control algorithm that may be designed using this output as the feedback signal.

Further, the learning gain, L, needs to be designed based on this synthesized output so that the ILC update law is stable in the iteration domain. To satisfy these objectives, the next section will prove that with a properly scaled output, $\tilde{y}(t)$, the proposed ROM is strictly output incremental passive, which allows the design of a stable learning gain L in a robust manner.

B. Strict Output-Incremental Passivity

Define the deviation variable x and output $\tilde{y}$,

$$x(t) = T(t) - T_{ss} \tag{7a}$$
$$\tilde{y}(t) = B(t)^T x(t), \tag{7b}$$

where T_{ss} is the solution to

$$0 = -DKD^T T_{ss} + K_{sub}(T_{sub} - T_{ss}) + H_\infty(T_\infty - T_{ss}). \tag{8}$$

Apply (7) and (8) in (4) we can have

$$C\dot{x}(t) = -Ax(t) + B(t)p(t) \tag{9a}$$
$$\tilde{y}(t) = B(t)^T x(t), \tag{9b}$$

where $A = DKD^T + K_{sub} + H_\infty$, A is positive definite, and $\tilde{y}(t)$ represents a weighted average of x from nodes that are encompassed by the circumference of laser beam. Next, this system is proved to be strictly output incremental passive using an approach similar to [20].

Proposition 1: The system described by (9) is strictly output incremental passive from the input p to output $\tilde{y}$, i.e., there exists $\lambda > 0$ such that $\langle \Delta p, \Delta\tilde{y} \rangle \geq \lambda \langle \Delta\tilde{y}, \Delta\tilde{y} \rangle$, with

$$\lambda = \frac{\lambda_{\min}(A)}{\max(B(t)^T B(t))}, \tag{10}$$

where $\lambda_{\min}(A)$ is the smallest eigenvalue of A, $\max(B^T B)$ is the maximum value of $B(t)^T B(t)$ as $B(t)$ is time-variant. (The inner product $\langle \cdot, \cdot \rangle$ is defined as $\langle f_1(\cdot), f_2(\cdot) \rangle = \int_0^{t_f} f_1(t) f_2(t) dt$.)

Proof: Define $\Delta x = x_1 - x_2$, $\Delta p = p_1 - p_2$, $\Delta\tilde{y} = \tilde{y_1} - \tilde{y_2}$, and the storage function $V = \frac{1}{2}\Delta x^T C \Delta x$. Then

$$\begin{aligned} \dot{V} &= \Delta x^T(-A\Delta x + B\Delta p) \\ &= -\Delta x^T A \Delta x + \Delta\tilde{y}^T \Delta p \end{aligned}$$

Note that

$$\Delta x^T A \Delta x \geq \lambda_{\min}(A) \Delta x^T \Delta x$$
$$\Delta\tilde{y}^T \Delta\tilde{y} = \Delta x^T B(t) B(t)^T \Delta x \leq \max(B(t)^T B(t)) \Delta x^T \Delta x,$$

Thus

$$\dot{V} \leq -\frac{\lambda_{\min}(A)}{\max(B(t)^T B(t))} \Delta\tilde{y}^T \Delta\tilde{y} + \Delta\tilde{y}^T \Delta p \tag{11}$$

We assume that the initial conditions for each iteration are identical, which sets $x_1(0) = x_2(0) = x_0$. Thus $V(0) = 0$ without loss of generality. Integrating both sides, we will have

$$0 \leq V \leq -\frac{\lambda_{\min}(A)}{\max(B(t)^T B(t))} \langle \Delta\tilde{y}, \Delta\tilde{y} \rangle + \langle \Delta\tilde{y}, \Delta p \rangle \tag{12}$$

Thus

$$\langle \Delta\tilde{y}, \Delta p \rangle \geq \frac{\lambda_{\min}(A)}{\max(B(t)^T B(t))} \langle \Delta\tilde{y}, \Delta\tilde{y} \rangle. \tag{13}$$

Thus, this system is strictly output incremental passive with

$$\lambda = \frac{\lambda_{\min}(A)}{\max(B(t)^T B(t))}. \tag{14}$$

■

Remark: Though B is time-variant, the shape of laser power defined by (5) is identical, thus $B(t)^T B(t)$ is constant. So the passivity bound λ can be simplified to:

$$\lambda = \frac{\lambda_{\min}(A)}{B(t)^T B(t)} \qquad \text{for any } t. \tag{15}$$

C. Passivity-based ILC Update Law

Based on the strictly output incremental passivity of the model, we can choose $\tilde{y}(t) = B(t)^T(T(t) - T_{ss})$ as the output in the proportional ILC update law. This choice of $\tilde{y}(t)$ is also reasonable to be calculated in a SLM machine since the thermal radiation in the laser's optical path is usually the only radiation that is recorded [21], [10], [22].

Correspondingly, the tracking error is $e(t) = \tilde{y_d}(t) - \tilde{y}(t) = B(t)^T(T_d(t) - T_{ss}) - B(t)^T(T(t) - T_{ss}) = B(t)^T(T_d(t) - T(t))$, thus T_{ss} is not needed in the ILC update law. Next, we show that the ILC update law (6) will converge with an appropriate learning gain L.

Theorem 2: Assume there exists an ideal input p_d such that the corresponding error $e_d = 0$. With ILC update law described in (6), $p_k \to p_d$ as $k \to \infty$ if

$$0 < L < 2\frac{k_{sub} + h_\infty}{B^T B}. \tag{16}$$

Proof: From the theorem in [20], p_k will converge to p_d as $k \to \infty$ if L is positive definite and $L < 2\lambda$. Recall (9), (15),

$$\lambda = \frac{\lambda_{\min}(A)}{B^T B} = \frac{\lambda_{\min}(DKD^T + K_{sub} + H_\infty)}{B^T B}. \tag{17}$$

Since $\lambda_{\min}(DKD^T + K_{sub} + H_\infty) = \lambda_{\min}(k_p DID^T + k_{sub} I + h_\infty I)$, thus

$$\lambda = \frac{k_{sub} + h_\infty}{B^T B} \tag{18}$$

Recall that $L \in R$, so a sufficient condition for the ILC update law described in (6) to be stable is

$$0 < L < 2\frac{k_{sub} + h_\infty}{B^T B}. \tag{19}$$

■

Remark This theorem provides a sufficient condition for the ILC update law to converge. In our FEM and ROM simulations, the heat transfer to the ambient atmosphere is ignored, so $T_{ss} = T_{sub}$ and the sufficient condition becomes:

$$0 < L < \frac{2k_{sub}}{B^T B}. \tag{20}$$

V. SIMULATION RESULTS

This section will first present results of parameter identification and validation the control oriented ROM against the high-fidelity FEM model. Then, the results of applying passivity-based ILC to both models will be examined. Finally, the ILC law will be tested on the FEM with melting.

A. Validation of ROM

To identify the parameters of the control oriented ROM in (4), a least squares system identification was performed from FEM generated input-output data. The data was generated from a simulation of a laser moving parallel to the x-axis while holding the laser power constant at $1\left[W\right]$.

The ROM simulation with these fitted parameters was performed with the same laser path and power in order to compare with the FEM simulation results (as verification). Fig. 4 presents a comparison of the outputs. The generated outputs, y_{ROM} and y_{FEM}, are in good agreement; verifying the performance of the ROM with respect to the FEM. However, there is a small and gradual divergence of the two outputs over time. This is most likely due to because the control-oriented ROM assumes that the substrate node is a pure heat sink, unlike the FEM model.

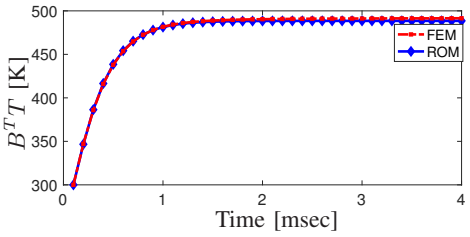

Fig. 4. Comparison of $y = B(t)^T T$ for FEM and ROM with constant 1[W] input for a straight laser raster line segment.

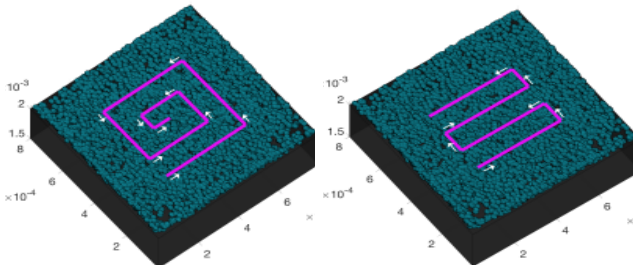

Fig. 5. Exact scale diagrams of the Spiral-in and zigzag paths used in the ROM and FEM simulations (scale is in $[m]$).

Since the ROM is capable of simulating arbitrary laser scan paths (Fig. 5) a spiral-in raster path on a $800\mu m$ x $800\mu m$ powderbed was chosen to validate the ROM (Fig. 6). Again, both the ROM and FEM use a constant laser power of $1\left[W\right]$. Also, note that for all used raster patterns the laser raster spacing is 87.5% of the laser spot diameter.

Initially, the extremely close match in Figure 4 is seen in Figure 6. Because the FEM model does not dissipate as much heat into the substrate as the ROM model, y_{FEM} increases relative to y_{ROM}. This effect compounds as the laser spot spirals inward, overlapping with areas recently heated by the laser. We note that adding additional node grid layers between the substrate node and the powder bed nodes would allow the ROM results to more closely match the FEM results, while increasing the complexity of the ROM.

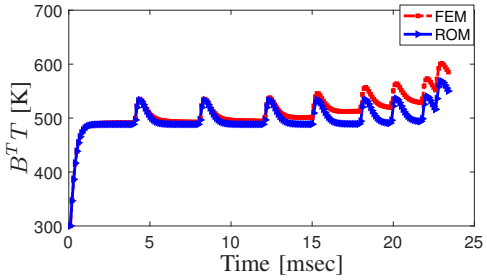

Fig. 6. Comparison of $y = B(t)^T T$ for FEM and ROM with constant 1[W] input and a spiral-in laser raster pattern.

Even so, the ROM matches the FEM fairly well, even when using a complex laser path. The largest $\|Error\|_2$ percentage for this comparison is 8.05%, where the scaled $\|Error\|_2$ is defined as:

$$\|Error\|_2 = \frac{\|B^T T_{FEM} - B^T T_{ROM}\|_2}{\|B^T T_{FEM}\|_2} \tag{21}$$

B. ILC Implementations and Comparison

Using the model parameters identified in the previous subsection, the sufficient condition (20) for choice of the proportional learning gain can be calculated as $0 < L < 0.0015$. Since the ROM is an informative analog for the FEM, a range of values from $0.002 - 0.012$ were chosen for L to be used in the learning law (6). These values were first tested on the control oriented ROM and subsequently implemented on the FEM. Each was implemented for 9 iterations. In addition, the sufficient condition, $L = 0.0015$, was tested on the ROM for completeness.

1) ILC simulation using the ROM: The previously discussed spiral-in raster path (Fig. 5) was again chosen to demonstrate that the ILC law (6) can be used to obtain an optimum laser power profile for a complex laser scan trajectory. A constant power of $2\left[W\right]$ is used for the initial (0^{th}) iteration. The desired output profile, y_d, is a constant temperature value for this case. Fig. 7 illustrates the output trajectory and the corresponding optimum laser power input after 9 iterations of learning. Figure 8a illustrates the evolution of the scaled output error norm ($\frac{\|e_k\|_2}{\sqrt{M}}$ against iteration number for a range of ILC gains, where $M = \frac{t_f}{T_s}$ and T_s is the sample time).

With sufficient iterations, $\frac{\|e_k\|_2}{\sqrt{M}}$ converges to values less than 22 $\left[K\right]$ (Fig. 8a) for all $L < 0.012$. Using $L = .008$ yields the fastest convergence rate and the lowest $\frac{\|e_k\|_2}{\sqrt{M}}$. Figure 7(b) shows the resulting output profile y_{ROM} using $L = .008$, and the close match to the desired output profile y_d. However, the effect of the laser changing direction cannot be completely eliminated.

2) ILC on FEM simulation of SLM without Melting: We now present results from simulation of the learning process on the FEM simulator. The results are indeed very similar to those obtained on the ROM discussed above, including $L = 0.008$ being the most optimal ILC gain

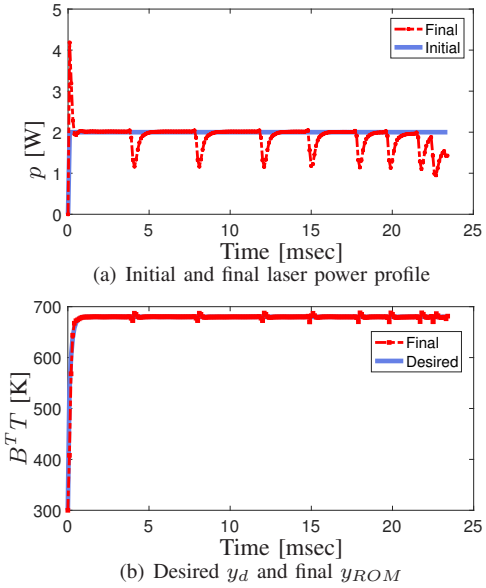

(a) Initial and final laser power profile

(b) Desired y_d and final y_{ROM}

Fig. 7. Resulting learned laser power profile and output after 9 ILC iterations using $L = .008$ for the spiral-in raster path on the output

(Fig. 9), as well as the qualitative shapes of the final output profiles(Fig. 10). This is notable considering the more complex temperature dynamics that are captured in the FEM. There are some interesting differences, though, which are highlighted below. It is unclear if $\frac{\|e_k\|_2}{\sqrt{M}}$ for $L = 0.01$ will asymptotically converge given more ILC iterations, and the error norm decrease is not monotonic. Also, even though $L = 0.008$ still asymptotes to the lowest $\frac{\|e_k\|_2}{\sqrt{M}}$, the convergence rate is not necessarily the fastest, unlike in the ROM case.

3) ILC on an FEM simulation of SLM with Melting: Even though the conditions for ILC convergence have not been discussed for a model that includes phase transitions, the ILC update law (6) was used on the FEM (with melting dynamics) for finding the optimal laser power profile for a zigzag raster pattern where the desired output, y_d, reaches weighted average temperatures above the melting temperature T_m for parts of the trajectory (Fig. 11). The yellow line segments in Figure 11 represent laser center positions where melting is desired. The desired output profile is shown as a solid line in Figure 12b. Note that y_d is extremely aggressive in comparison to the previous desired output for the spiral-in case (Fig. 10b). $L = .008$ was chosen as the learning gain, as before.

For the initial iteration (Fig. 12a), the laser power was set to $18\left[W\right]$ when the laser center is in the yellow line regions of Figure 11 and turned off otherwise. After the 9^{th} iteration an optimized laser power profile was obtained. The evolution of the scaled output error norm $\frac{\|e_k\|_2}{\sqrt{M}}$ against iterations is shown in Fig. 13. It is interesting to note that this rror $\frac{\|e_k\|_2}{\sqrt{M}}$ is more than an order of magnitude greater than the spiral-in case shown in Figure 9. The bulk of the error accrues when y_d prescribes a value that is too low given the large amount of thermal mass previously imparted into powderbed when

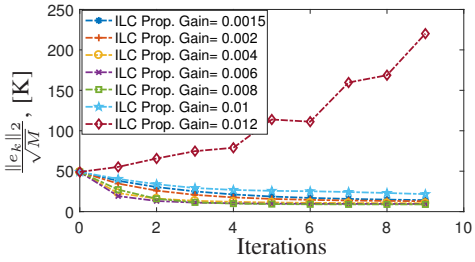

(a) All simulated ILC gains

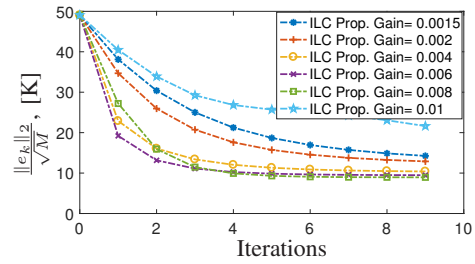

(b) All asymptotic ILC gains

Fig. 8. Evolution of scaled error norm $\frac{\|e\|_2}{\sqrt{M}}$ against iterations, for the spiral-in raster path scenario

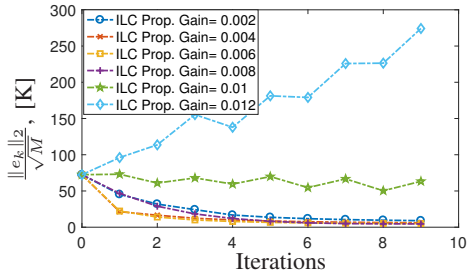

(a) Error evolution for all simulated ILC gains

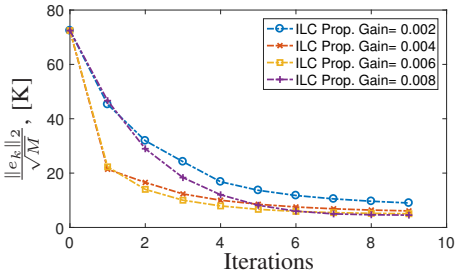

(b) Error evolution for stable ILC gains

Fig. 9. Convergence of FEM $\frac{\|e\|_2}{\sqrt{M}}$ using $L = \{.002 - .012\}$ for the spiral-in raster path

the laser was turned on (Fig. 12b). More simply put, the local regions of the powderbed are not able to cool fast enough for the output profile y_{FEM} to follow the desired profile y_d.

In addition, after the second and fourth change in laser direction, an artifact in the y_{FEM} profile appears. There is noticeable change in negative slope as y_{FEM} decreases. This change in slope corresponds to the laser changing direction. These artifacts are the same as the dramatic changes in y_{FEM} observed in Figure 6 where the laser is staying in similar locations to where laser power was absorbed.

The results shown in Figure 13 demonstrate that ILC can indeed be used for optimizing laser power profiles in SLM.

VI. CONCLUSION

In this manuscript, a control oriented ROM that captures single layer, below-melting temperature dynamics was proposed. Based on this model, an approach to designing ILC algorithms was presented that exploits the passivity of the control oriented ROM. The implementation of the ILC law was successfully demonstrated on both the ROM and FEM, which additionally validated the convergence. The ILC update law showed good tracking and convergence performance. Error convergence for the ROM and FEM were remarkably similar for many of the tested ILC gains, which supports the fact that the proposed ROM can be used as a good reference during the design of ILC update laws for real SLM processing. Finally, the use of the ILC law was extended to FEM simulations including melting where good tracking and convergence performance was still observed.

ACKNOWLEDGMENT

This work was supported in part by the U.S. Department of Energy, Office of Science, Office of Advanced Scientific Computing Research, under Award Number DE-SC-0011327 and in part by the National Science Foundation Career Award grant CMMI-1254313. High performance computing aspects of the work were performed with support from SCOREC at RPI. We thank Professor Mario Juha of the Universidad de La Sabana for his input.

REFERENCES

[1] S. Bremen, W. Meiners, and A. Diatlov, "Selective laser melting," *Laser Technik Journal*, vol. 9, no. 2, pp. 33–38, 2012.

[2] P. Mercelis and J.-P. Kruth, "Residual stresses in selective laser sintering and selective laser melting," *Rapid Prototyping Journal*, vol. 12, no. 5, pp. 254–265, 2006.

[3] S. Das, "Physical aspects of process control in selective laser sintering of metals," *Advanced Engineering Materials*, vol. 5, no. 10, pp. 701–711, 2003.

[4] J. Mazumder, "Overview of melt dynamics in laser processing," *Optical engineering*, vol. 30, no. 8, pp. 1208–1219, 1991.

[5] P. Fischer, V. Romano, H.-P. Weber, N. Karapatis, E. Boillat, and R. Glardon, "Sintering of commercially pure titanium powder with a nd: Yag laser source," *Acta Materialia*, vol. 51, no. 6, pp. 1651–1662, 2003.

[6] S. Roy, M. Juha, M. S. Shephard, and A. M. Maniatty, "Heat transfer model and finite element formulation for simulation of selective laser melting," *Computational Mechanics*, 2017.

[7] A. V. Gusarov, I. Yadroitsev, P. Bertrand, and I. Smurov, "Heat transfer modelling and stability analysis of selective laser melting," *Applied Surface Science*, vol. 254, no. 4, pp. 975–979, 2007.

[8] F. Verhaeghe, T. Craeghs, J. Heulens, and L. Pandelaers, "A pragmatic model for selective laser melting with evaporation," *Acta Materialia*, vol. 57, no. 20, pp. 6006–6012, 2009.

[9] G. Tapia and A. Elwany, "A review on process monitoring and control in metal-based additive manufacturing," *Journal of Manufacturing Science and Engineering*, vol. 136, no. 6, p. 060801, 2014.

[10] J.-P. Kruth, P. Mercelis, J. Van Vaerenbergh, and T. Craeghs, "Feedback control of selective laser melting," in *Proceedings of the 3rd international conference on advanced research in virtual and rapid prototyping*, 2007, pp. 521–527.

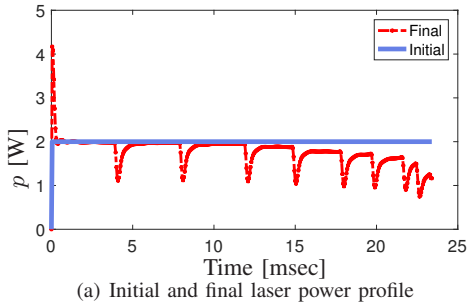

(a) Initial and final laser power profile

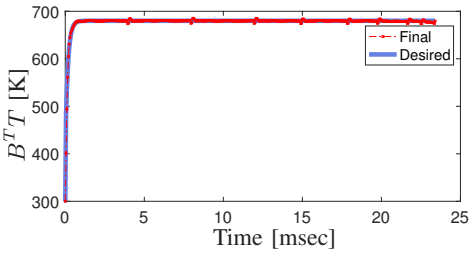

(b) Desired y_d and final y_{FEM}

Fig. 10. Resulting FEM laser power profile and output after 9 ILC iterations using $L = .008$ for the spiral-in raster path.

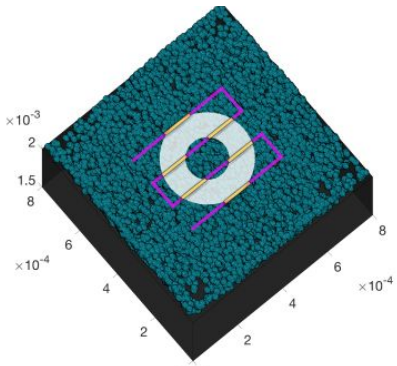

Fig. 11. Schematic of zig-zag raster for melting a ring (scale is in $[m]$).

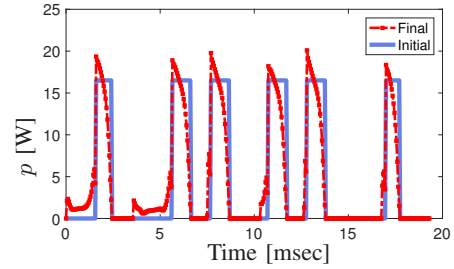

(a) Initial and final iteration FEM laser power profiles.

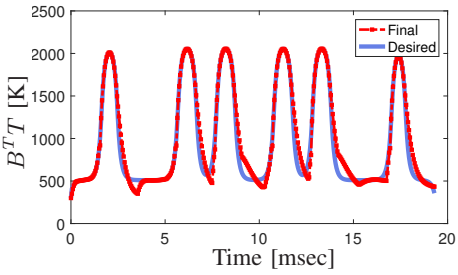

(b) Desired y_d and final y_{FEM}

Fig. 12. Resulting FEM laser power profile and output after 9 ILC iterations using $L = .008$ for the concentric cylinder trajectory.

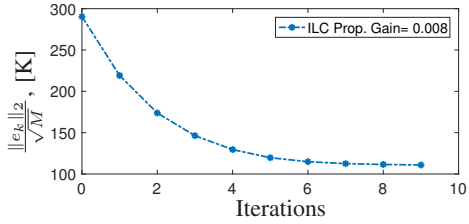

Fig. 13. Plot of $\frac{\|e\|_2}{\sqrt{M}}$ against iterations for demonstrating ILC on an FEM simulation scenario with melting.

[11] T. Craeghs, F. Bechmann, S. Berumen, and J.-P. Kruth, "Feedback control of layerwise laser melting using optical sensors," *Physics Procedia*, vol. 5, pp. 505–514, 2010.

[12] S. M. Thompson, L. Bian, N. Shamsaei, and A. Yadollahi, "An overview of direct laser deposition for additive manufacturing; part i: Transport phenomena, modeling and diagnostics," *Additive Manufacturing*, vol. 8, pp. 36–62, 2015.

[13] Q. Wang, J. Li, M. Gouge, A. R. Nassar, P. Michaleris, and E. W. Reutzel, "Reduced-order multivariable modeling and nonlinear control of melt-pool geometry and temperature in directed energy deposition," in *American Control Conference (ACC), 2016*. IEEE, 2016, pp. 845–851.

[14] P. M. Sammons, D. A. Bristow, and R. G. Landers, "Iterative learning control of bead morphology in laser metal deposition processes," in *American Control Conference (ACC), 2013*. IEEE, 2013, pp. 5942–5947.

[15] X. Cao and B. Ayalew, "Control-oriented mimo modeling of laser-aided powder deposition processes," in *American Control Conference (ACC), 2015*. IEEE, 2015, pp. 3637–3642.

[16] P. M. Sammons, D. A. Bristow, and R. G. Landers, "Control-oriented modeling of laser metal deposition as a repetitive process," in *American Control Conference (ACC), 2014*. IEEE, 2014, pp. 1817–1820.

[17] D. A. Bristow, M. Tharayil, and A. G. Alleyne, "A survey of iterative learning control," *IEEE Control Systems*, vol. 26, no. 3, pp. 96–114, 2006.

[18] D. J. Hoelzle, A. G. Alleyne, and A. J. W. Johnson, "Basis task approach to iterative learning control with applications to micro-robotic deposition," *IEEE Transactions on Control Systems Technology*, vol. 19, no. 5, pp. 1138–1148, 2011.

[19] L. Parry, I. Ashcroft, and R. D. Wildman, "Understanding the effect of laser scan strategy on residual stress in selective laser melting through thermo-mechanical simulation," *Additive Manufacturing*, vol. 12, pp. 1–15, 2016.

[20] R. Quintanilla and J. T. Wen, "Passivity based iterative learning control for mechanical systems subject to dry friction," in *2008 American Control Conference*. IEEE, 2008, pp. 4573–4578.

[21] Y. Chivel and I. Smurov, "On-line temperature monitoring in selective laser sintering/melting," *Physics Procedia*, vol. 5, pp. 515–521, 2010.

[22] P. Lott, H. Schleifenbaum, W. Meiners, K. Wissenbach, C. Hinke, and J. Bültmann, "Design of an optical system for the in situ process monitoring of selective laser melting (slm)," *Physics Procedia*, vol. 12, pp. 683–690, 2011.